Continuous-variable multipartite vibrational entanglement

Mehdi Abdi◉*

Department of Physics, Isfahan University of Technology, Isfahan 84156-83111, Iran

A compact scheme for the preparation of macroscopic multipartite entanglement is proposed and analyzed. In this scheme, the vibrational modes of a mechanical resonator constitute continuous-variable (CV) subsystems that entangle with each other as a result of their interaction with a two-level system (TLS). By properly driving the TLS, we show that a selected set of modes can be activated and prepared in a multipartite entangled state. We first study the entanglement properties of a three-mode system by evaluating the genuine multipartite entanglement, and we investigate its usefulness as a quantum resource by computing the quantum Fisher information. Moreover, the robustness of the state against the qubit and thermal noises is studied, proving a long-lived entanglement. To examine the scalability and structural properties of the scheme, we derive an effective model for the multimode system through elimination of the TLS dynamics. This work provides a step toward a compact and versatile device for creating a multipartite noise-resilient entangled state in vibrational modes as a resource for CV quantum metrology, quantum communication, and quantum computation.

I. INTRODUCTION

Quantum entanglement is a pivotal resource in many quantum technologies, from quantum communications [1–3] and quantum computations [4–6], to quantum metrology where the Heisenberg limit is approached only by employing a multipartite entangled state [7–9]. Meanwhile, as mechanical systems have proven to be very efficient in weak force sensing both at the macroscopic level [10,11] and mesoscopic scales [12,13], the quantum sensing thus would require investigations on the entangled mechanical oscillators [14–20]. From a different perspective, the entangled mechanical resonators can serve as nodes of a quantum network [21–23].

Interaction of the mechanical resonators with other quantum systems such as optical cavities [24–26], electronic [27,28], and spin degrees of freedom [29] opens an avenue for employing their vibrational modes for quantum information processing [30–33]. An opposite route is to use the mechanical resonators for controlling [34–37] or intermediating interactions among other physical systems [38,39]. Such schemes have already been sought and used for developing scalable quantum networks [40,41]. In either case, the size of the system can be considerably miniaturized— compared to the electromagnetic counterparts—due to the smaller wavelength and stationary nature of the vibrational modes. Multimode optomechanical systems have been investigated from various points of view both theoretically [42–44] and experimentally [45–48]. Recently, multimode circuit quantum acoustodynamical (cQAD) systems based on bulk [49–51] and surface [52–56] acoustic resonators have been subject to intense research, propelling toward scalable quantum information with vibrational modes [57–61].

In this work, we put forth a scheme that allows for creating multipartite vibrational entangled states in a controllable way via their coupling to a two-level system (TLS). Instead of several mechanical systems, we propose to employ the normal modes of a single resonator, thus significantly reducing the spatial extent, complexity, and noise of the system. The TLS serves to mediate a controllable interaction between the modes. The scheme is in principle implementable in surface acoustic wave (SAW) cavities and high overtone bulk acoustic resonators (HBARs) coupled to superconducting qubits in a cQAD system [62,63], or it can be envisaged in other setups such as flexural modes of a membrane combined with an embedded optically active lattice defect [64,65]. Here, we study a regime where the TLS decay rate dominates its coupling to the vibrational modes, and we show that the TLS can be adiabatically eliminated from the system dynamics to obtain a network of effectively interacting modes with an adjustable interaction structure. The latter is achieved by modulating the drive frequency of the TLS at the eigenfrequencies of a set of vibrational modes; see Fig. 1. We show that a multipartite entangled state of CV systems is attainable under experimentally realizable conditions, and we study its robustness against the system noises. Furthermore, by computing the quantum Fisher information (QFI) of the state, we prove that these states are useful for enhanced quantum sensing at the Heisenberg limit, e.g., for detection of gravitational waves and dark matter evidence [66–68].

II. MODEL

The frequency spectrum $\{\omega_k\}$ $(k = 1, 2, \ldots, N)$ of the vibrational eigenmodes of a mechanical resonator are determined by its geometrical properties [65,69]. These vibrational degrees-of-freedom can couple to a two-level system in various schemes, e.g., a superconducting qubit through
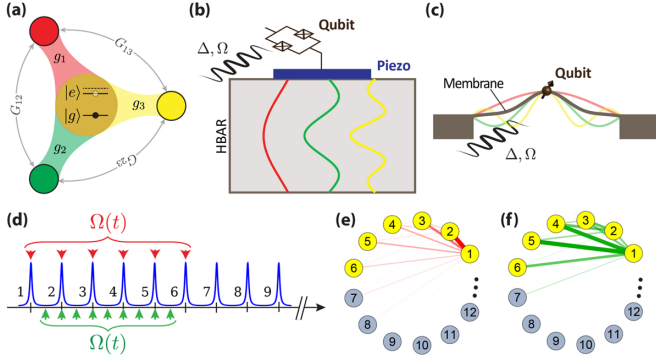
*mehabdi@gmail.com

FIG. 1. (a) A TLS coupled to multiple vibrational modes of a mechanical resonator can intermediate their mutual interactions, which allows for creating a multipartite entangled state among those modes. This can be implemented, e.g., in (b) an HBAR whose longitudinal modes couple to a superconducting qubit via a piezoelectric device, or (c) the flexural modes of a membrane interacting with an embedded-atom-like defect. (d) In a multimode scheme, the set of modes are *activated* (here 1–6) by employing properly modulated drives that form two-mode squeezing interactions. The interaction is shown as a graph for two different modulation schemes: at the mode frequencies (e) and the half-sum frequencies (f). The edge thickness represents the interaction strength, while the *active* modes are highlighted in yellow.

piezoelectric effects in a cQAD device [62], or the electronic spin two-level system of an embedded optically active lattice defect [70–74]. The dynamics of the system is governed by the Hamiltonian

$$\hat{H} = \tfrac{1}{2}(\Delta\hat{\sigma}_z + \Omega\hat{\sigma}_x) + \sum_{k=1}^{N}[\omega_k\hat{b}_k^\dagger\hat{b}_k + \tfrac{1}{2}g_k\hat{\sigma}_z(\hat{b}_k + \hat{b}_k^\dagger)], \quad (1)$$

where $\hat{\sigma}_x$ and $\hat{\sigma}_z$ are the Pauli matrices of a TLS driven with a Rabi frequency Ω and at detuning Δ. The vibrational modes are expressed by the phonon annihilation (creation) operators $\hat{b}_k$ ($\hat{b}_k^\dagger$) with the nontrivial canonical commutation relation $[\hat{b}_k, \hat{b}_l^\dagger] = \delta_{kl}$. The dimensionless canonical operators of each mode are related to these bosonic operators through $\hat{b}_k = (\hat{x}_k + i\hat{p}_k)/\sqrt{2}$ such that $[\hat{x}_k, \hat{p}_l] = i\delta_{kl}$.

Before moving to the full analysis of the system, we qualitatively discuss how the Hamiltonian in Eq. (1) leads to the entanglement of vibrational modes. Interaction of the TLS with the spectrum of the mechanical modes leads to their mutual interactions [Fig. 1(a)]. This can be readily seen by adiabatic elimination of the TLS from the equations of motion. The process is valid when the TLS decay rate Γ is greater than its coupling strength to any mechanical mode of interest; for details, see Appendix A. We also assume that the TLS is driven at far off-resonance ($\Delta \gg \Gamma, \Omega$), and we apply a proper polaron transformation [75]. The resulting interaction Hamiltonian is not in resonance with the desired interactions, and thus it does not provide appreciable entanglements. To "activate" the interactions, we propose to modulate the TLS drive $\Omega(t) = \Omega_0 \sum_i \cos(w_i t)$ at the proper frequencies w_j [33,76]. This brings us to the following interaction Hamiltonian after applying a rotating-wave approximation

(RWA):

$$\hat{H}_{\rm RWA} = \tfrac{1}{2}\sum_{k,l} G_{k,l}\big(B_{k,l}^{\rm tms}\hat{b}_k\hat{b}_l - B_{k,l}^{\rm qst}\hat{b}_k\hat{b}_l^\dagger\big) + {\rm H.c.}, \quad (2)$$

where $G_{k,l}$ is the effective coupling rate, and $B^{\rm tms}$ and $B^{\rm qst}$ are the weighted adjacency matrices that determine the strength of two-mode squeezing and quantum state transfer interactions, respectively; see Appendix B for the details. When the mechanical spectrum has noncommensurate frequencies, any desired subset of modes are activated by setting $\{w_i\} \subseteq \{\omega_k\}$ with the cardinality ${\rm card}\{w_i\} = M$, where M is the number of *active* modes. In the language of graphs, the system forms a complete-graph. Such interactions with enough strength lead to a state that is equivalent to a multipartite CV GHZ-state [77–80]. In a commensurate spectrum, the other modes get involved in the interactions by the same choice of modulation frequencies. However, their coupling strength is smaller than the *active* modes, and it contributes only negligibly to the entanglement dynamics [Fig. 1(e)]. Alternatively, one modulates the drive at half of the mode sum frequencies $w_i = \tfrac{1}{2}(\omega_k + \omega_l)$ to get a better connected graph [Fig. 1(f)]. Nonetheless, the numerical results suggest that the effect is incremental at the cost of a more complicated modulation.

In a HBAR cQAD device, the longitudinal modes of a bulk acoustic wave cavity with high-quality factors couple to a superconducting qubit through a piezoelectric interface; see, e.g., [51]. The HBAR modes form a spectrum of equally spaced frequencies $\omega_k = k\delta_{\rm FSR}$ ($k = 1, 2, \dots$) with free spectral range $\delta_{\rm FSR}$ that is determined by the cavity length and medium, hence forming a commensurate spectrum. A few techniques can be envisaged for introducing anharmonicity to the mode spacing [61], and thus enhancing the efficiency of the activating protocol. However, here we set our focus on the simple commensurate setup for experimental feasibility and concreteness.

III. TRIANGLE SYSTEM

The full system is described by Hamiltonian (1) where the nonlinear essence of the qubit gives rise to non-Gaussianity of the mechanical state. As the simplest network, first we investigate a triangle, i.e., a system made of three lowest vibrational modes (Fig. 1). The dynamics is described by the quantum optical master equation

$$\dot{\rho} = \frac{i}{\hbar}[\rho, \hat{H}] + \frac{\Gamma}{2}\big\{(\bar{n}_{\omega_q} + 1)\mathcal{D}_{\hat{\sigma}_-}[\rho] + \bar{n}_{\omega_q}\mathcal{D}_{\hat{\sigma}_+}[\rho]\big\} + \frac{\widetilde{\Gamma}}{2}\mathcal{D}_{\hat{\sigma}_z}[\rho]$$

$$+ \tfrac{1}{2}\sum_{k=1}^{3}\gamma_k\big\{(\bar{n}_{\omega_k} + 1)\mathcal{D}_{\hat{b}_k}[\rho] + \bar{n}_{\omega_k}\mathcal{D}_{\hat{b}_k^\dagger}[\rho]\big\}, \quad (3)$$

where the Lindblad superoperators are $\mathcal{D}_{\hat{o}}[\rho] \equiv 2\hat{o}\rho\hat{o}^\dagger - \hat{o}^\dagger\hat{o}\rho - \rho\hat{o}^\dagger\hat{o}$. Here, ω_q is the TLS level splitting, while Γ and $\widetilde{\Gamma}$ are the qubit relaxation and decoherence rate, respectively. The mechanical damping rates are $\gamma_k \equiv \omega_k/Q$ with the quality factor Q. The bosonic thermal occupation number at temperature T is $\bar{n}_\omega = (\exp\{\hbar\omega/k_B T\} - 1)^{-1}$ with the Boltzmann constant k_B. In our analysis, we assume that the mechanical modes as well as the TLS are initialized in their ground
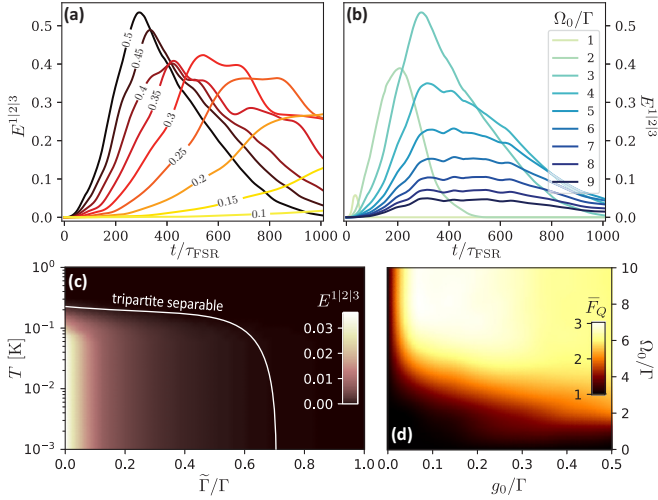
FIG. 2. Time evolution of the TPE (a) for different coupling rates (the curve labels show g_0/Γ) at the Rabi frequency $\Omega_0 = 3\Gamma$, and (b) for different Rabi frequencies at $g_0 = 0.5\Gamma$. (c) Robustness of longtime $E^{1|2|3}$: Density plot showing the tripartite entangled and separable parameter regions vs reservoir temperature and TLS pure dephasing rate $\widetilde{\Gamma}$ evaluated at $t = 1000\tau_{\text{FSR}}$ for $\Omega_0 = 7\Gamma$ and $g_0 = 0.5\Gamma$. (d) The maximum normalized QFI as a function of coupling strength and drive amplitude.

state by some cooling mechanism [73,74], and a modulated electromagnetic drive excites the TLS.

In numerical evaluation of Eq. (3), we consider a vibrational spectrum with $\delta_{\text{FSR}}/2\pi = 20$ MHz and $Q = 10^7$ interacting with the TLS ($\omega_q/2\pi = 10$ GHz and $\Gamma/2\pi = 20$ MHz) with coupling rates $g_k = g_0 \lesssim \Gamma$, δ_{FSR} [48,51,55,81]. Unless specified otherwise, we take a dilation refrigerator temperature of $T = 10$ mK for the reservoir, set $\Delta = 5\Omega_0$ to obtain $\langle \hat{\sigma}_z \rangle \approx -1$ to ensure effective coupling between the mechanical modes, and assume an ideal TLS, $\widetilde{\Gamma} = 0$. By choosing an optimal value for the drive power Ω_0 and coupling strengths, a long-lived tripartite mechanical entangled state is attained that sustains the qubit and thermal noise for thousands of the longest mechanical period, $\tau_{\text{FSR}} \equiv 2\pi/\delta_{\text{FSR}}$, which is hundreds of nanoseconds.

The results are summarized in Fig. 2, where we present the genuine multipartite entanglement $E^{1|2|3}$ and the normalized quantum Fisher information $\overline{F}_Q$ as defined in Refs. [82,83] and given in Appendix E. In Fig. 2(a), the time evolution of the entanglement in the three-mode system is plotted for different coupling rates, while in Fig. 2(b) its evolution is shown for various drive amplitudes. The entanglement curves exhibit a fast rise followed by a rapid decay for large coupling rates and/or low Rabi frequencies, which survives for several hundreds of oscillations. Remarkably, in the opposite regime (weaker g_0 and/or higher Ω_0) the system is dragged toward a quasistationary tripartite entanglement (TPE). To study the robustness of the entanglement against TLS pure dephasing as well as the thermal noise at higher temperatures, we take the $E^{1|2|3}$ for $g_0 = 0.5\Gamma$ and $\Omega_0 = 7\Gamma$ at $t = 1000\tau_{\text{FSR}}$ as a representative long-living TPE and show the effect of these two major sources of noise in Fig. 2(c). Interestingly, the system remains tripartite entangled, though fragile, for a wide

range of noise parameters. In higher temperatures, TLS thermalization is the main source of decoherence. In a setup with a high enough ω_q, TPE survives even up to $T \sim 10$ K, where the mechanical noise destroys the entanglement (not shown). Finally, we compute the maximum QFI in measuring the collective mechanical position $\hat{X}_3 = \sum_{i=1}^3 \hat{x}_i$ in our scheme, and we study its dependence on the coupling strength g_0 and Rabi frequency Ω_0 [Fig. 2(d)]. The results suggest that the QFI increases by operating at high coupling strengths and drive amplitudes. Interestingly, the maximum QFI even reaches the Heisenberg limit $\overline{F}_Q = 3$, which means at least 1.73 times enhancement in the sensitivity compared to a separable state is obtained for moderate g_0 values. It is worth mentioning here that the mechanical entangled state is non-Gaussian thanks to the nonlinear nature of the TLS. Note that non-Gaussianity is a crucial feature for universal quantum computation with continuous-variable systems. This is confirmed by computing the entropy distance of the density matrix from a reference Gaussian state as discussed in Appendix E.

IV. MULTIPARTITE ENTANGLED STATE

It is computationally expensive to study systems with a larger number of modes through (3) since it becomes memory-intensive. Therefore, to expand our investigations to larger systems, and to test our strategy for generating a multipartite entangled state, we employ an effective Gaussian model. The effective model is derived for both the Hamiltonian and the TLS-induced noise and damping on the mechanical modes through adiabatic elimination of the TLS. Thanks to its Gaussian nature, the system is thus fully characterized by the covariance matrix (CM) V when displaced to the mean values of the canonical operators. To find the dynamics of the CM, one forms a vector of quadrature operators $\mathbf{u} = [\hat{x}_1, \hat{p}_1, \ldots, \hat{x}_M, \hat{p}_M]^\mathsf{T}$ and derives the quantum Langevin equation of its elements; see Appendix C for the details. In the compact form one gets $\dot{\mathbf{u}} = -A\mathbf{u} + \mathbf{n}$, where $\mathbf{n}$ is the vector of noise operators, and the time-dependent drift matrix is given by

$$A(t) = \begin{bmatrix} \frac{1}{2}\kappa_1 & -\omega_1 & \cdots & 0 & 0 \\ \omega_1 + G_{1,1}(t) & \frac{1}{2}\kappa_1 & \cdots & G_{1,M}(t) & 0 \\ \vdots & \vdots & \ddots & \vdots & \vdots \\ 0 & 0 & \cdots & \frac{1}{2}\kappa_M & -\omega_M \\ G_{M,1}(t) & 0 & \cdots & \omega_M + G_{M,M}(t) & \frac{1}{2}\kappa_M \end{bmatrix},$$

$$(4)$$

where $G_{k,l}(t) \equiv \frac{1}{2\Delta(2\bar{n}_{\omega_q}+1)} \frac{g_k g_l}{\omega_k \omega_l} \Omega(t)^2$ is the coupling strength of the modes to each other in the effective model. Here, $\kappa_k = \gamma_k + \widetilde{\gamma}_k$ is the total damping rate composed of the intrinsic γ_k and the TLS-induced damping rates $\widetilde{\gamma}_k \equiv g_k^2 [\mathcal{S}(\omega_k) - \mathcal{S}(-\omega_k)]$, with $\mathcal{S}(\omega)$ the TLS steady-state fluctuation spectrum [75]. The CM of the system is readily computed via the following equation:

$$\dot{V} = AV + VA^\mathsf{T} + D, \qquad (5)$$

where D is the diffusion matrix, i.e., the matrix of noise correlators [84,85]. In this work, we assume that the noises are Gaussian and Markovian. This brings us to $D = \bigoplus_{k=1}^M D_k$
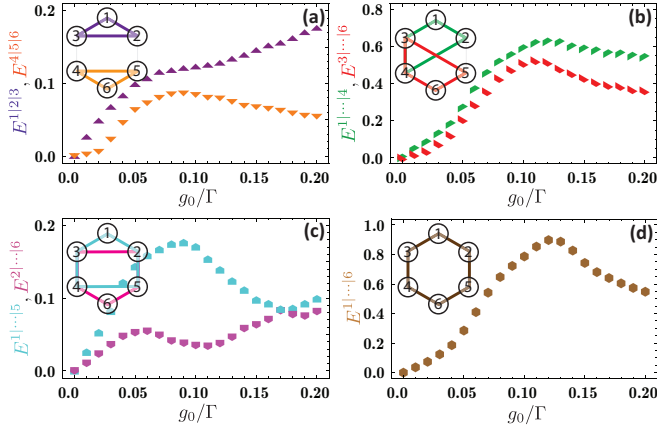
FIG. 3. Genuine N-partite entanglement for a set of six modes as a function of the coupling strength g_0 at $\Omega_0 = 3\Gamma$ and $t = 1000\tau_{\mathrm{FSR}}$: (a) $N = 3$, (b) $N = 4$, (c) $N = 5$, and (d) $N = 6$.

with $D_k \equiv [\gamma_k(\bar{n}_{\omega_k} + \frac{1}{2}) + \widetilde{\gamma}_k(\tilde{n}_{\omega_k} + \frac{1}{2})]I_2$, where I_2 is a 2×2 identity matrix. The effective TLS-induced occupancy is calculated by $\tilde{n}_\omega \equiv \mathcal{S}(-\omega)/[\mathcal{S}(\omega) - \mathcal{S}(-\omega)]$.

The chosen set of parameters ensures the validity of the TLS adiabatic elimination. The convergence and reliability of the numerical results are verified as outlined in Appendix D. We restrict our analysis to $M = 6$, as this is the maximum number of modes that we can afford given the computational resources. The genuine N-partite entanglement values ($3 \leqslant N \leqslant 6$) are evaluated at $t = 1000\tau_{\mathrm{FSR}}$ as a function of g_0 and presented in Fig. 3. Two sets for the $N = 3, 4, 5$ cases are studied: the set of modes closest to the fundamental mode and those that gather around the farthest modes. Since the effective coupling rate $G_{k,l}$ is proportional to the inverse mode frequencies, the fundamental mode has the strongest coupling to the active modes. From this perspective, the stronger entanglement exhibited in the first set with an almost monotonic growth with the coupling rate is intuitive. Therefore, the fundamental mode plays a central role in the structure of the entangled cluster. We should emphasize that the system is originally nonlinear, and thus one expects a non-Gaussian essence in the above-discussed multimode mechanical states that is not perceptible in our Gaussian effective model.

V. SCALABILITY

The fundamental mode is central in the entanglement structure of our scheme and at the same time it is the most vulnerable mode to the thermal noise. Therefore, it is crucial to learn about the depth of its influence in the vibrational spectrum. In other words, how strongly does it entangle to the higher-order modes of the resonator, and how robust is it? Hence, we single out the fundamental and kth modes to study their bipartite entanglement $E^{1|k}$ [Fig. 4(a)]. The logarithmic negativity [86] of the bipartite system of $\rho_{\mathcal{H}_1 \otimes \mathcal{H}_k}$ is evaluated for 100 modes at $t = 1000\tau_{\mathrm{FSR}}$ as a function of g_0 when the qubit is excited by a drive modulated at ω_1 and ω_k. In Fig. 4(b) the residual entanglement, the parameter region where $E^{1|k} > 0$, is presented at different temperatures. The
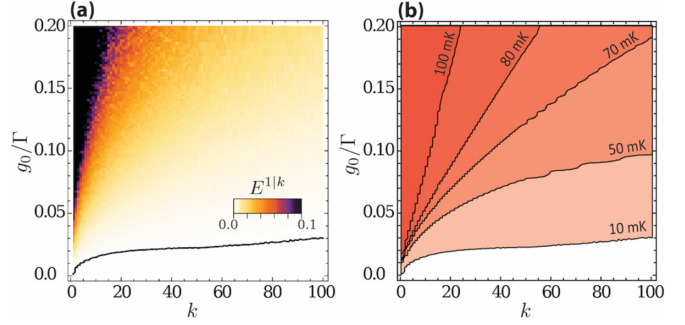

FIG. 4. The bipartite entanglement between the fundamental mode and the kth mode $E^{1|k}$ as a function of coupling rate g_0: (a) Logarithmic negativity at $T = 10$ mK. (b) The entangled regions at five different temperatures. In both plots, the values correspond to $\Omega_0 = 3\Gamma$ at $t = 1000\tau_{\mathrm{FSR}}$.

modes with lower frequencies assume stronger entanglement to the fundamental mode as expected. Remarkably, by increasing the temperature, they retain their entanglement quite firmly, with a small change in the amount (not shown). Meanwhile, the high-frequency modes preserve their entanglement with the fundamental mode, provided the coupling strength to the intermediating TLS g_0 is large enough.

VI. SUMMARY AND CONCLUSION

To summarize, we have introduced and studied a compact and versatile device for creating a network of continuous-variable multipartite entangled states. The vibrational modes of a single resonator constitute nodes of the network. These modes are coupled and entangled as a result of their interaction with a driven-dissipative two-level system. We have proposed to activate a desired set of modes by modulating the TLS drive tone at their respective frequencies. This results in a long-living noise-resilient genuine multipartite entangled state that is useful for quantum metrology as the QFI of their state shows. We have also studied the structure of entanglement for a hexagon network, proving the central role of the fundamental mode in the network. Finally, the influence of the fundamental mode on the mechanical spectrum shows that at the cryogenic temperatures, hundreds of modes can join the network.

ACKNOWLEDGMENTS

APPENDIX A: ADIABATIC ELIMINATION

In this Appendix, we present the details of our procedure in deriving the effective Hamiltonian (2) starting from the original Hamiltonian (1). We start by removing the qubit-mechanical interaction by applying the polaron transformation $\hat{U} = \exp\{\frac{1}{2}i\hat{\sigma}_z\hat{P}\}$ with the collective dimensionless

momentum [87]

$$\hat{P} = -i \sum_k \frac{g_k}{\omega_k} (\hat{b}_k - \hat{b}_k^\dagger). \tag{A1}$$

We are then brought to

$$\hat{U}\hat{H}\hat{U}^\dagger = \frac{\Delta}{2}\hat{\sigma}_z + \frac{\Omega}{2}\big(\hat{\sigma}_+ e^{-i\hat{P}} + \hat{\sigma}_- e^{+i\hat{P}}\big) + \sum_k \omega_k \hat{b}_k^\dagger \hat{b}_k, \tag{A2}$$

where we have discarded a constant term.

The adiabatic elimination is performed by assuming that the qubit decay rate is larger than its coupling strength to any of the mechanical modes $\Gamma \gg \{g_k\}$. In this regime, the total density matrix can be approximated by $\rho(t) \simeq \rho_{\text{TLS}}(t) \otimes \rho_{\text{Mec}}(t)$. Therefore, a mean-field approximation becomes applicable. Then the following equations describe the qubit dynamics [88]:

$$\langle\dot{\hat{\sigma}}_+\rangle = -\Big(\frac{\Gamma}{2}\big(2\bar{n}_{\omega_q} + 1\big) - i\Delta\Big)\langle\hat{\sigma}_+\rangle - \frac{1}{2}i\Omega e^{+i\langle\hat{P}\rangle}\langle\hat{\sigma}_z\rangle, \tag{A3a}$$

$$\langle\dot{\hat{\sigma}}_-\rangle = -\Big(\frac{\Gamma}{2}\big(2\bar{n}_{\omega_q} + 1\big) + i\Delta\Big)\langle\hat{\sigma}_-\rangle + \frac{1}{2}i\Omega e^{-i\langle\hat{P}\rangle}\langle\hat{\sigma}_z\rangle, \tag{A3b}$$

$$\langle\dot{\hat{\sigma}}_z\rangle = -\Gamma\Big(1 + \big(2\bar{n}_{\omega_q} + 1\big)\langle\hat{\sigma}_z\rangle\Big) \\ - i\Omega\big(\langle\hat{\sigma}_+\rangle e^{-i\langle\hat{P}\rangle} - \langle\hat{\sigma}_-\rangle e^{+i\langle\hat{P}\rangle}\big), \tag{A3c}$$

where for the sake of simplicity an ideal qubit with no pure dephasing $\widetilde{\Gamma} = 0$ is assumed. The solutions to the above equations in qubit steady states, i.e., the states with $\langle\hat{\sigma}_\pm\rangle_{\text{ss}} = \langle\hat{\sigma}_z\rangle_{\text{ss}} = 0$, are

$$\langle\hat{\sigma}_\pm\rangle_{\text{ss}} = \frac{\pm i\Omega\big(\Gamma\big(2\bar{n}_{\omega_q} + 1\big) \mp 2i\Delta\big)e^{\pm i\langle\hat{P}\rangle}}{\big(2\bar{n}_{\omega_q} + 1\big)\big(\Gamma^2\big(2\bar{n}_{\omega_q} + 1\big)^2 + 4\Delta^2 + 2\Omega^2\big)}, \tag{A4a}$$

$$\langle\hat{\sigma}_z\rangle_{\text{ss}} = \frac{-\Gamma^2\big(2\bar{n}_{\omega_q} + 1\big)^2 + 4\Delta^2}{\big(2\bar{n}_{\omega_q} + 1\big)\big(\Gamma^2\big(2\bar{n}_{\omega_q} + 1\big)^2 + 4\Delta^2 + 2\Omega^2\big)}. \tag{A4b}$$

A simple set of equations is found by operating the system at the far-detuned regime where $\Delta \gg \Gamma, \Omega$,

$$\langle\hat{\sigma}_\pm\rangle_{\text{ss}} \approx \frac{\Omega}{2\Delta\big(2\bar{n}_{\omega_q} + 1\big)}e^{\pm i\langle\hat{P}\rangle}, \tag{A5a}$$

$$\langle\hat{\sigma}_z\rangle_{\text{ss}} \approx -1. \tag{A5b}$$

By plugging these in (A2) for the qubit operators, we arrive at

$$\hat{H}_{\text{ad}} = \sum_k \omega_k \hat{b}_k^\dagger \hat{b}_k + \frac{\Omega^2}{2\Delta\big(2\bar{n}_{\omega_q} + 1\big)}\cos(\hat{P} - \langle\hat{P}\rangle), \tag{A6}$$

after discarding a constant shift in the energy. This Hamiltonian is valid for the above-discussed regime and adequately addresses the system dynamics after the TLS passes its transient dynamics $t > \Gamma^{-1}$. The collective momentum then is expected to exhibit small fluctuations around its mean value

$\text{Tr}\{(\hat{P} - \langle\hat{P}\rangle)\rho_{\text{Mec}}(t)\} \ll 1$. This allows us to expand the cosine and keep up to the quadratic terms

$$\cos(\hat{P} - \langle\hat{P}\rangle) \approx 1 - \tfrac{1}{2}(\hat{P} - \langle\hat{P}\rangle)^2 = 1 - \tfrac{1}{2}(\hat{P}^2 + \langle\hat{P}\rangle^2 - 2\langle\hat{P}\rangle\hat{P}).$$

The second term in the parentheses gives a constant energy, while the third causes a shift in the phase space. We skip both and write

$$\hat{H}_{\text{ad}} \approx \sum_k \omega_k \hat{b}_k^\dagger \hat{b}_k + \frac{1}{2}\sum_{k,l} G_{k,l}(\hat{b}_k\hat{b}_l - \hat{b}_k\hat{b}_l^\dagger + \text{H.c.}), \tag{A7}$$

where the effective coupling rate is

$$G_{k,l} \equiv \frac{\Omega^2}{2\Delta\big(2\bar{n}_{\omega_q} + 1\big)}\frac{g_k g_l}{\omega_k \omega_l}. \tag{A8}$$

To check the validity of the mean-field approximation in the discussed regime, we numerically solve the qubit equations in (A3) replacing $\hat{P}$ with a real number, and we compare the results with the solution of quantum optical master equation (3). In Fig. 5, the two solutions are compared against each other. One clearly verifies that the solutions are very close in the adiabatic elimination regime.

On the dissipation side of the dynamics, the TLS-mechanical interaction causes extra dissipation in the mechanical modes. This is formulated effectively through second-order perturbation theory [89]. The additional damping rate for each mechanical mode is then $\widetilde{\gamma}_k \equiv g_k^2[\mathcal{S}(\omega_k) - \mathcal{S}(-\omega_k)]$. According to the quantum dissipation-fluctuation theorem, there is an accompanying thermal noise with occupation number $\tilde{n}_{\omega_k} \equiv \mathcal{S}(-\omega_k)/[\mathcal{S}(\omega_k) - \mathcal{S}(-\omega_k)]$. Here, the TLS steady-state fluctuation spectrum is given by

$$\mathcal{S}(\omega) = \tfrac{1}{2}\text{Re}\int_0^\infty ds\big[\langle\hat{\sigma}_z(s)\hat{\sigma}_z(0)\rangle_{\text{ss}} - \langle\hat{\sigma}_z\rangle_{\text{ss}}^2\big]e^{i\omega s}. \tag{A9}$$

The spectrum is evaluated using the quantum regression theorem [88]. The resulting expression is cumbersome. Therefore, we only summarize the equations that lead to it along the same lines as Ref. [75]. We express the spectrum of TLS as $\mathcal{S}(\omega) = \tfrac{1}{2}\text{Re}\{C_3(s = -i\omega)\}$, where C_3 is the third element of the following vector:

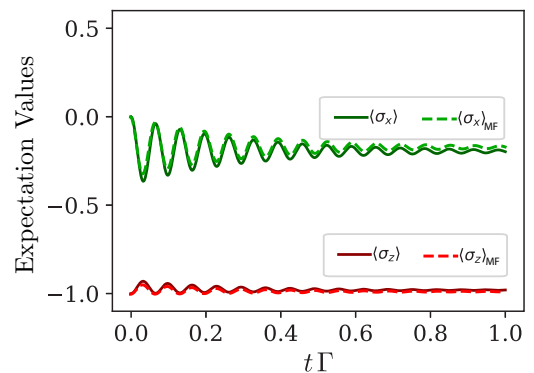$$\mathbf{C}(s) = (sI - M)^{-1}\mathbf{v}, \tag{A10}$$

FIG. 5. Comparison of the expectations values for the TLS operators: the exact (solid lines) vs mean-field approximation (dashed lines), which are solutions to Eqs. (A3). See the text for details.

where I is a 3×3 identity matrix, and the matrix M and vector $\mathbf{v}$ are defined through Eqs. (A3) and their steady-state solutions as

$$M = \begin{pmatrix} -\frac{1}{2}\Gamma(2\bar{n}_{\omega_q}+1) + \widetilde{\Gamma} + i\Delta & 0 & -\frac{1}{2}i\Omega \\ 0 & -\frac{1}{2}\Gamma(2\bar{n}_{\omega_q}+1) + \widetilde{\Gamma} - i\Delta & +\frac{1}{2}i\Omega \\ -i\Omega & i\Omega & -\Gamma(2\bar{n}_{\omega_q}+1) \end{pmatrix}, \quad \mathbf{v} = \begin{pmatrix} -\langle\hat{\sigma}_+\rangle_{\mathrm{ss}}(1+\langle\hat{\sigma}_z\rangle_{\mathrm{ss}}) \\ +\langle\hat{\sigma}_-\rangle_{\mathrm{ss}}(1-\langle\hat{\sigma}_z\rangle_{\mathrm{ss}}) \\ 1 - \langle\hat{\sigma}_z\rangle_{\mathrm{ss}}^2 \end{pmatrix}. \quad \text{(A11)}$$

These noises and TLS-induced damping are taken into account in studying the dynamics of an effective fully mechanical system; see Appendix C.

APPENDIX B: ROTATING WAVE APPROXIMATION

The Hamiltonian (A7) provides us with interactions of two-mode squeezing and state-transfer between all modes, and thus it is potentially rich for quantum information processing purposes. However, none of the above interactions are on resonance. This becomes clear by moving to the interaction picture of $\hat{H}_0 = \sum_k \omega_k \hat{b}_k^\dagger \hat{b}_k$. In this Appendix, we show that a selected set of modes can resonantly be brought into the desired interaction by applying a modulated drive to the qubit, i.e., by replacing the Ω with

$$\Omega(t) = \Omega_0 \sum_i \cos w_i t, \quad \text{(B1)}$$

with properly chosen modulation frequencies w_i that will become clear shortly. To show this, we move to the interaction picture of $\hat{H}_0$ and arrive at

$$\widetilde{H}_{\mathrm{ad}} \approx \frac{1}{2}\sum_{k,l} G_{k,l}(t)\left[\hat{b}_k\hat{b}_l e^{-i(\omega_k+\omega_l)t} - \hat{b}_k\hat{b}_l^\dagger e^{-i(\omega_k-\omega_l)t} + \mathrm{H.c.}\right],$$

where now $G_{k,l}$ are time-dependent through the Rabi frequency; see Eq. (A8). The drive in (B1) then gives us

$$\Omega(t)^2 = \Omega_0^2 \sum_{i,j} \cos(w_i t)\cos(w_j t)$$
$$= \frac{1}{2}\Omega_0^2 \sum_{i,j}\left\{\cos[(w_i+w_j)t] + \cos[(w_i-w_j)t]\right\}$$
$$= \frac{1}{4}\Omega_0^2 \sum_{i,j}\left[e^{i(w_i+w_j)t} + e^{i(w_i-w_j)t} + \mathrm{c.c.}\right].$$

In the numerical analysis that is performed in the manuscript for multimode systems larger than three, we use Hamiltonian (A7) and derive the Langevin equations; see Appendix C. Nonetheless, it is instructive to see how a time-dependent drive can link the mechanical modes to each other. Therefore, by setting the above equation back in $\widetilde{H}_{\mathrm{ad}}$ and performing a rotating-wave approximation (RWA), only a few of the mode interactions can survive. When the mode frequencies are *noncommensurate*, the desired set of modes with frequencies $\{\omega_k\}$ can be *activated* by simply setting $w_k = \omega_k$ for any set of modes. This gives

$$\hat{H}_{\mathrm{RWA}} = \frac{1}{2}\sum_{k,l}^M G_{k,l}\hat{p}_k\hat{p}_l, \quad \text{(B2)}$$

where $G_{k,l}$ is the same as (A8) but with Ω replaced by Ω_0. Note that the interaction with and among the rest of the

spectrum becomes counterrotating and thus is ignored. An alternative modulation strategy is to drive at half of the sum frequencies such that $w_i = \omega_{k,l} := \frac{1}{2}(\omega_k + \omega_l)$. In this case, the effective Hamiltonian in the RWA is in the following form:

$$\hat{H}'_{\mathrm{RWA}} = \frac{1}{4}\sum_{k,l}^M G_{k,l}(\hat{x}_k\hat{x}_l + \hat{p}_k\hat{p}_l). \quad \text{(B3)}$$

Concerning the two-mode squeezing interaction, both schemes result in the same interaction graphs, as is conceived from Fig. 6.

Nevertheless, in our proposed setup the set of mode frequencies $\{\omega_k\}$ are commensurate. This indeed involves a few undesired modes in the system dynamics. Another cause of the commensurate spectrum is that the coupling rate coefficients become weighted as some interactions receive drive from other drive tones. Therefore, the RWA Hamiltonian in our setup becomes

$$\hat{H}_{\mathrm{RWA}} = \frac{1}{2}\sum_{k,l} G_{k,l}\left(B_{k,l}^{\mathrm{tms}}\hat{b}_k\hat{b}_l - B_{k,l}^{\mathrm{qst}}\hat{b}_k\hat{b}_l^\dagger + \mathrm{H.c.}\right), \quad \text{(B4)}$$

where B^{tms} and B^{qst} are the adjacency matrices of the two-mode squeezing and quantum state-transfer interactions, respectively. Figure 7 shows the weight of each interaction via an illustrative presentation of the matrix elements of the adjacency matrix $\mathcal{F}_{k,l} \equiv G_{k,l}B_{k,l}^{\mathrm{tms}}$ for two different modulation schemes described above. We notice that even though the modulated drive is tuned for a set of target modes (the green square), the other modes are also connected (the blue square). By taking into account the inverse frequencies that appear in the interaction strengths, the effect of these higher modes becomes negligible. This is indeed also shown as the graphs in Fig. 1 in the main text.
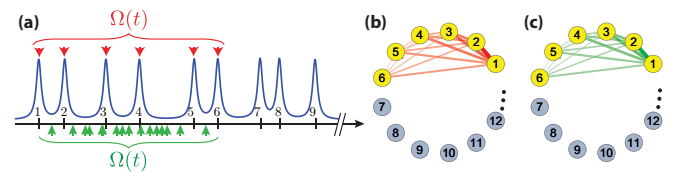

FIG. 6. (a) When the spectrum is noncommensurate, any desired set of modes can be activated by simply modulating the TLS drive on their frequencies (red arrows) or at half of the sum frequencies (green arrows). The activated modes form a complete graph, though weighted, for the two-mode squeezing interaction in both modulation strategies as illustrated for (b) mode frequencies modulation and (c) half of the sum frequencies modulation.
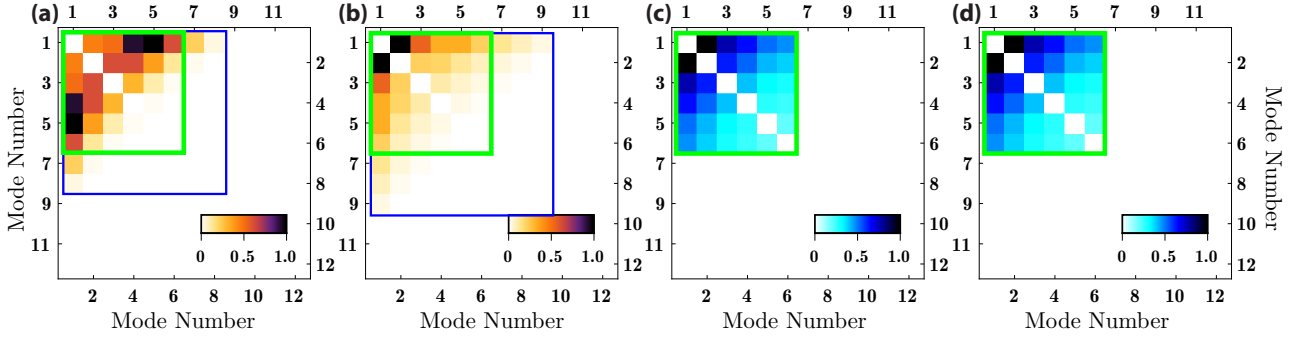
FIG. 7. Normalized matrix elements of the effective two-mode squeezing coupling matrices $\mathcal{F}_{k,l}$: (a) and (b) for the commensurate spectrum with modulations at half sum frequencies and mode frequencies, respectively. In (c) and (d) the same are shown for a noncommensurate spectrum. The green square highlights the *target* set of modes, whereas the blue square illustrates the set of *activated* modes that are directly coupled to the target set.

APPENDIX C: MECHANICAL LANGEVIN EQUATIONS

The Hamiltonian (A7) is Gaussian and allows us to study the system dynamics through the covariance matrix of the mechanical canonical operators. The quantum Langevin equations (QLEs) include the effect of the environment on the dynamics of the system operators used to obtain the time evolution of the covariance matrix. We find the following QLEs for the motion of the mechanical modes:

$$\dot{b}_k = -(\tfrac{1}{2}\kappa_k + i\omega_k)\hat{b}_k - i\sum_l G_{k,l}(t)(\hat{b}_l + \hat{b}_l^\dagger) + \hat{\xi}_k, \quad \text{(C1)}$$

where $\kappa_k \equiv \gamma_k + \widetilde{\gamma}_k$ is the total damping rate stemming from the support, γ_k, and the TLS decoherences, $\widetilde{\gamma}_k$, as discussed in Appendix A. The total noise operator is also divided into the support noise and the TLS-induced noise $\hat{\xi}_k \equiv \sqrt{\gamma_k}\hat{b}_k^{\text{in}} + \sqrt{\widetilde{\gamma}_k}\widetilde{b}_k^{\text{in}}$. Assuming that the intrinsic motional noise is Markovian, the noise operator has the following nonvanishing correlation functions:

$$\langle\hat{\xi}_k(t)\hat{\xi}_l^\dagger(t')\rangle = \left[\gamma_k\left(\overline{n}_{\omega_k} + 1\right) + \widetilde{\gamma}_k\left(\widetilde{n}_{\omega_k} + 1\right)\right]\delta(t - t')\delta_{kl}, \tag{C2a}$$

$$\langle\hat{\xi}_k^\dagger(t)\hat{\xi}_l(t')\rangle = \left[\gamma_k\overline{n}_{\omega_k} + \widetilde{\gamma}_k\widetilde{n}_{\omega_k}\right]\delta(t - t')\delta_{kl}. \tag{C2b}$$

By forming a vector of Hermitian operators $\mathbf{u} \equiv [\hat{x}_1, \hat{p}_1, \ldots, \hat{x}_M, \hat{p}_M]^{\mathsf{T}}$, one arrives at the following compact form of Eqs. (C1):

$$\dot{\mathbf{u}} = A\mathbf{u} + \mathbf{n}, \tag{C3}$$

where A is given by (4), and $\mathbf{n} = [\hat{\xi}_1^x, \hat{\xi}_1^p, \ldots, \hat{\xi}_M^x, \hat{\xi}_M^p]$ is the vector of noise operators with $\hat{\xi}_k \equiv (\hat{\xi}_k^x + i\hat{\xi}_k^p)/\sqrt{2}$. The covariance matrix dynamics is readily calculated from (C3) as Eq. (5) in the main text [85].

APPENDIX D: NUMERICAL METHOD

To perform the numerical integration over the quantum optical master equation (3), we use the QuTiP package [90]. The Hilbert space $\mathcal{H}$ truncation was done by minimizing the error. Our estimation for the error by tracking the convergence curve shows that for a truncation at $\dim\{\mathcal{H}\} = 2 \times 10 \times 9 \times 8$, an approximate error of $\approx 1.73\%$ is committed, which is the minimum possible error given the computational resources at hand.

The study of the original Hamiltonian with more than three mechanical modes is not feasible because of the huge demands for the computational memories. We therefore have opted to use the Gaussian effective Hamiltonian, which is valid in the regime discussed in Appendixes A and C. To
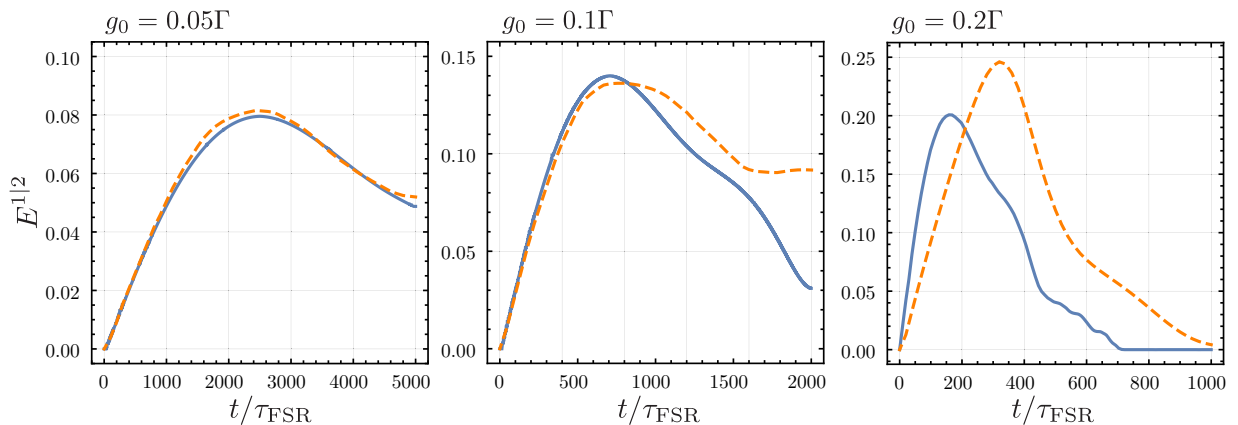

FIG. 8. Comparison of the entanglement $E^{1|2}$ as an illustration of the consistency: the original Hamiltonian (dashed orange) vs the effective Hamiltonian (solid blue) for three different coupling strengths. Here, $\Omega_0 = 1\Gamma$ and the other parameters are the same as in the main text.
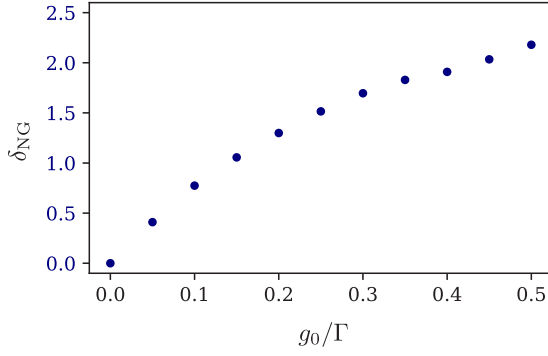
FIG. 9. The non-Gaussianity of the triangle system vs coupling strength. The parameters are given in the main text. Here, we set $\Omega_0 = 3\Gamma$ and evaluate the measure of non-Gaussianity at $t = 1000\tau_{\mathrm{FSR}}$.

numerically prove its validity, we compare the results obtained from (3) and (5). In Fig. 8, the bipartite entanglement $E^{1|2}$ obtained from the original and effective models is plotted for three different coupling strength values. The results confirms that the behavior of both models coincides for weak-coupling strengths. This is indeed as one would expect, as the adiabatic elimination is valid when the TLS arrives at its quasisteady state. The deviation emerges as the coupling rate assumes higher values, such that the effective model overestimates the TLS-induced decoherence.

APPENDIX E: ENTANGLEMENT, QUANTUM FISHER INFORMATION, AND NON-GAUSSIANITY

In this Appendix, we deal with the details of the entanglement properties, represent the measures used in the main text, and study the non-Gaussianity of the entangled state.

To analyze the entanglement structure of the system, we first show that our scheme indeed leads to a GHZ-state. For the sake of clarity and simplicity, the case of noncommensurate modes for which the interaction is pure $\hat{p}_k \hat{p}_l$ is discussed; see Eq. (B2). The results are easily generalized to a system with a commensurate mode spectrum. In the interaction picture, after a time interval t, the Hamiltonian (B2) transforms the canonical operators as

$$\hat{x}_k \rightarrow \hat{x}_k - t \sum_l G_{k,l} \hat{p}_l, \tag{E1a}$$

$$\hat{p}_k \rightarrow \hat{p}_k. \tag{E1b}$$

The effective coupling constant $G_{k,l}$ is inversely proportional to the mode frequencies $G_{k,l} \propto (\omega_k \omega_l)^{-1}$. Therefore, the mode with the lowest frequency couples more strongly to the other nodes in the network (Fig. 6). This suggests a star-shaped graph for the network with the lowest mode at the center. Therefore, the position transformations can be approximately simplified to

$$\hat{x}_1 \rightarrow \hat{x}_1 - \sum_k \chi_k \hat{p}_k$$

for the "first" mode and

$$\hat{x}_k \rightarrow \hat{x}_k - \chi_k \hat{p}_1$$

for the rest with $\chi_k \equiv t G_{1,k}$. The entanglement of a state is not affected by local unitary transformations. Hence, after a local $\pi/2$ rotation on the first mode, one gets $\hat{x}_1 \rightarrow \hat{p}_1$ and $\hat{p}_1 \rightarrow -\hat{x}_1$. Then it is easy to verify that the state of the system at a given time t becomes such that

$$\sum_{k=1}^{M} \hat{p}_k(t) = \sum_{k=1}^{M} \hat{p}_k(0) e^{-\chi_k}, \tag{E2a}$$

$$\hat{x}_k(t) - \hat{x}_l(t) = \hat{x}_k(0) e^{-\chi_k} - \hat{x}_l(0) e^{-\chi_l}, \tag{E2b}$$

with $k, l = 1, 2, \ldots M$. After a long enough drive, one has $\chi_k \rightarrow \infty$, where the system reaches a Greenberger-Horne-Zeilinger (GHZ) entangled state [77,79].

We use the genuine multipartite entanglement measure introduced in Ref. [82] to quantify the entanglement in our system. The measure exploits the monogamy property of the entanglement such that

$$E^{1|2,3,\ldots,M} = \sum_{j=2}^{M} E^{1|j} + \sum_{k>j}^{M} \sum_{j=2}^{M} E^{1|j|k} + \cdots + E^{\underline{1}|2|\cdots|M},$$

where the underline denotes the *focus* party, and E is a proper measure of entanglement [91]. The genuine residual N-partite entanglement is then calculated as the minimum over all permutations of the subsystem indices,

$$E^{1|2|\cdots|M} \equiv \min\{E^{\underline{i_1}|i_2|\cdots|i_M}\}. \tag{E3}$$

The quantum Fisher information determines the Cramer-Rao bound in parameter estimation and saturates to the Heisenberg limit for a fully entangled system [9]. Hence, it reflects the degree of multipartite entanglement [92–94]. For a mixed state ρ and observable $\hat{O}$, the QFI is defined as

$$F_Q[\rho, \hat{O}] = 2 \sum_{k,l} |\langle k|\hat{O}|l\rangle|^2 \frac{(\lambda_k - \lambda_l)^2}{\lambda_k + \lambda_l}, \tag{E4}$$

where λ_k and $|k\rangle$ are the eigenvalues and eigenvectors of ρ, respectively. The sum is over indices in which $\lambda_k + \lambda_l > 0$ [83]. Here, we take the collective mechanical position $\hat{X}_M \equiv \sum_{k=1}^{M} \hat{x}_k$ as the observable and introduce $\overline{F}_Q \equiv \frac{1}{M} F_Q$, the normalized QFI. This quantity is then upper-bounded by M for a fully entangled system.

Finally, in order to examine the non-Gaussian nature of the entangled state in the triangle system, we compute the non-Gaussianity measure of the state using the one introduced in Ref. [95]: δ_{NG} of a given state ρ is defined as the distance of its entropy from a reference Gaussian state ρ_G: $\delta_{\mathrm{NG}} \equiv S(\rho_G) - S(\rho)$, where $S(\rho) = -\mathrm{Tr}\{\rho \ln \rho\}$ is the von Neumann entropy. The measure of non-Gaussianity is computed for the mechanical state $\rho_{\mathrm{m}} \equiv \mathrm{Tr}_{\mathrm{TLS}}\{\rho\}$, where $\mathrm{Tr}_{\mathrm{TLS}}$ denotes a partial trace over the TLS. In Fig. 9, the measure is shown as a function of coupling strength g_0 for the triangle system. As expected, the non-Gaussianity of the state increases with the coupling rate.

[1] C. H. Bennett, G. Brassard, C. Crépeau, R. Jozsa, A. Peres, and W. K. Wootters, Teleporting an Unknown Quantum State Via Dual Classical and Einstein-Podolsky-Rosen Channels, Phys. Rev. Lett. **70**, 1895 (1993).

[2] S. L. Braunstein and H. J. Kimble, Teleportation of Continuous Quantum Variables, Phys. Rev. Lett. **80**, 869 (1998).

[3] H. J. Kimble, The quantum internet, Nature (London) **453**, 1023 (2008).

[4] D. P. DiVincenzo, Quantum computation, Science **270**, 255 (1995).

[5] S. Lloyd and S. L. Braunstein, Quantum Computation Over Continuous Variables, Phys. Rev. Lett. **82**, 1784 (1999).

[6] N. C. Menicucci, P. van Loock, M. Gu, C. Weedbrook, T. C. Ralph, and M. A. Nielsen, Universal Quantum Computation with Continuous-Variable Cluster States, Phys. Rev. Lett. **97**, 110501 (2006).

[7] D. J. Wineland, J. J. Bollinger, W. M. Itano, F. L. Moore, and D. J. Heinzen, Spin squeezing and reduced quantum noise in spectroscopy, Phys. Rev. A **46**, R6797(R) (1992).

[8] S. F. Huelga, C. Macchiavello, T. Pellizzari, A. K. Ekert, M. B. Plenio, and J. I. Cirac, Improvement of Frequency Standards with Quantum Entanglement, Phys. Rev. Lett. **79**, 3865 (1997).

[9] V. Giovannetti, S. Lloyd, and L. Maccone, Advances in quantum metrology, Nat. Photon. **5**, 222 (2011).

[10] G. Binnig, C. F. Quate, and C. Gerber, Atomic Force Microscope, Phys. Rev. Lett. **56**, 930 (1986).

[11] H. B. Chan, V. A. Aksyuk, R. N. Kleiman, D. J. Bishop, and F. Capasso, Quantum mechanical actuation of microelectromechanical systems by the Casimir force, Science **291**, 1941 (2001).

[12] E. Gavartin, P. Verlot, and T. J. Kippenberg, A hybrid on-chip optomechanical transducer for ultrasensitive force measurements, Nat. Nanotechnol. **7**, 509 (2012).

[13] J. Moser, J. Güttinger, A. Eichler, M. J. Esplandiu, D. E. Liu, M. I. Dykman, and A. Bachtold, Ultrasensitive force detection with a nanotube mechanical resonator, Nat. Nanotechnol. **8**, 493 (2013).

[14] J. Eisert, M. B. Plenio, S. Bose, and J. Hartley, Towards Quantum Entanglement in Nanoelectromechanical Devices, Phys. Rev. Lett. **93**, 190402 (2004).

[15] M. B. Plenio, J. Hartley, and J. Eisert, Dynamics and manipulation of entanglement in coupled harmonic systems with many degrees of freedom, New J. Phys. **6**, 36 (2004).

[16] S. Pirandola, D. Vitali, P. Tombesi, and S. Lloyd, Macroscopic Entanglement by Entanglement Swapping, Phys. Rev. Lett. **97**, 150403 (2006).

[17] J. D. Jost, J. P. Home, J. M. Amini, D. Hanneke, R. Ozeri, C. Langer, J. J. Bollinger, D. Leibfried, and D. J. Wineland, Entangled mechanical oscillators, Nature (London) **459**, 683 (2009).

[18] M. Abdi, S. Pirandola, P. Tombesi, and D. Vitali, Entanglement Swapping with Local Certification: Application to Remote Micromechanical Resonators, Phys. Rev. Lett. **109**, 143601 (2012).

[19] C. F. Ockeloen-Korppi, E. Damskägg, J.-M. Pirkkalainen, M. Asjad, A. A. Clerk, F. Massel, M. J. Woolley, and M. A. Sillanpää, Stabilized entanglement of massive mechanical oscillators, Nature (London) **556**, 478 (2018).

[20] R. Riedinger, A. Wallucks, I. Marinković, C. Löschnauer, M. Aspelmeyer, S. Hong, and S. Gröblacher, Remote quantum entanglement between two micromechanical oscillators, Nature (London) **556**, 473 (2018).

[21] M. Schmidt, M. Ludwig, and F. Marquardt, Optomechanical circuits for nanomechanical continuous variable quantum state processing, New J. Phys. **14**, 125005 (2012).

[22] S. Rips and M. J. Hartmann, Quantum Information Processing with Nanomechanical Qubits, Phys. Rev. Lett. **110**, 120503 (2013).

[23] S. Zippilli and D. Vitali, Dissipative Engineering of Gaussian Entangled States in Harmonic Lattices with a Single-Site Squeezed Reservoir, Phys. Rev. Lett. **126**, 020402 (2021).

[24] D. Vitali, S. Gigan, A. Ferreira, H. R. Böhm, P. Tombesi, A. Guerreiro, V. Vedral, A. Zeilinger, and M. Aspelmeyer, Optomechanical Entanglement Between a Movable Mirror and a Cavity Field, Phys. Rev. Lett. **98**, 030405 (2007).

[25] M. Paternostro, D. Vitali, S. Gigan, M. S. Kim, C. Brukner, J. Eisert, and M. Aspelmeyer, Creating and Probing Multipartite Macroscopic Entanglement with Light, Phys. Rev. Lett. **99**, 250401 (2007).

[26] I. Favero and K. Karrai, Optomechanics of deformable optical cavities, Nat. Photon. **3**, 201 (2009).

[27] M. Blencowe, Quantum electromechanical systems, Phys. Rep. **395**, 159 (2004).

[28] M. Abdi, M. Pernpeintner, R. Gross, H. Huebl, and M. J. Hartmann, Quantum State Engineering with Circuit Electromechanical Three-Body Interactions, Phys. Rev. Lett. **114**, 173602 (2015).

[29] D. Lee, K. W. Lee, J. V. Cady, P. Ovartchaiyapong, and A. C. B. Jayich, Topical review: spins and mechanics in diamond, J. Opt. **19**, 033001 (2017).

[30] M. J. Hartmann and M. B. Plenio, Steady State Entanglement in the Mechanical Vibrations of Two Dielectric Membranes, Phys. Rev. Lett. **101**, 200503 (2008).

[31] P. Rabl, S. J. Kolkowitz, F. H. L. Koppens, J. G. E. Harris, P. Zoller, and M. D. Lukin, A quantum spin transducer based on nanoelectromechanical resonator arrays, Nat. Phys. **6**, 602 (2010).

[32] K. Stannigel, P. Rabl, A. S. Sørensen, P. Zoller, and M. D. Lukin, Optomechanical Transducers for Long-Distance Quantum Communication, Phys. Rev. Lett. **105**, 220501 (2010).

[33] M. Abdi and M. J. Hartmann, Entangling the motion of two optically trapped objects via time-modulated driving fields, New J. Phys. **17**, 013056 (2015).

[34] E. R. MacQuarrie, T. A. Gosavi, N. R. Jungwirth, S. A. Bhave, and G. D. Fuchs, Mechanical Spin Control of Nitrogen-Vacancy Centers in Diamond, Phys. Rev. Lett. **111**, 227602 (2013).

[35] A. Barfuss, J. Teissier, E. Neu, A. Nunnenkamp, and P. Maletinsky, Strong mechanical driving of a single electron spin, Nat. Phys. **11**, 820 (2015).

[36] M. J. A. Schuetz, E. M. Kessler, G. Giedke, L. M. K. Vandersypen, M. D. Lukin, and J. I. Cirac, Universal Quantum Transducers Based on Surface Acoustic Waves, Phys. Rev. X **5**, 031031 (2015).

[37] S. Maity, L. Shao, S. Bogdanović, S. Meesala, Y.-I. Sohn, N. Sinclair, B. Pingault, M. Chalupnik, C. Chia, L. Zheng, K. Lai, and M. Lončar, Coherent acoustic control of a single silicon vacancy spin in diamond, Nat. Commun. **11**, 193 (2020).

[38] S. D. Bennett, N. Y. Yao, J. Otterbach, P. Zoller, P. Rabl, and M. D. Lukin, Phonon-Induced Spin-Spin Interactions in

Diamond Nanostructures: Application to Spin Squeezing, Phys. Rev. Lett. **110**, 156402 (2013).

[39] A. Albrecht, A. Retzker, F. Jelezko, and M. B. Plenio, Coupling of nitrogen vacancy centres in nanodiamonds by means of phonons, New J. Phys. **15**, 083014 (2013).

[40] M.-A. Lemonde, S. Meesala, A. Sipahigil, M. J. A. Schuetz, M. D. Lukin, M. Loncar, and P. Rabl, Phonon Networks with Silicon-Vacancy Centers in Diamond Waveguides, Phys. Rev. Lett. **120**, 213603 (2018).

[41] A. H. Safavi-Naeini, D. V. Thourhout, R. Baets, and R. V. Laer, Controlling phonons and photons at the wavelength scale: integrated photonics meets integrated phononics, Optica **6**, 213 (2019).

[42] A. Xuereb, C. Genes, and A. Dantan, Strong Coupling and Long-Range Collective Interactions in Optomechanical Arrays, Phys. Rev. Lett. **109**, 223601 (2012).

[43] X.-W. Xu, Y.-J. Zhao, and Y.-X. Liu, Entangled-state engineering of vibrational modes in a multimembrane optomechanical system, Phys. Rev. A **88**, 022325 (2013).

[44] H. Seok, L. F. Buchmann, E. M. Wright, and P. Meystre, Multimode strong-coupling quantum optomechanics, Phys. Rev. A **88**, 063850 (2013).

[45] A. B. Shkarin, N. E. Flowers-Jacobs, S. W. Hoch, A. D. Kashkanova, C. Deutsch, J. Reichel, and J. G. E. Harris, Optically Mediated Hybridization Between Two Mechanical Modes, Phys. Rev. Lett. **112**, 013602 (2014).

[46] L. Fan, K. Y. Fong, M. Poot, and H. X. Tang, Cascaded optical transparency in multimode-cavity optomechanical systems, Nat. Commun. **6**, 5850 (2015).

[47] W. H. P. Nielsen, Y. Tsaturyan, C. B. Møller, E. S. Polzik, and A. Schliesser, Multimode optomechanical system in the quantum regime, Proc. Natl. Acad. Sci. (USA) **114**, 62 (2017).

[48] P. Arrangoiz-Arriola, E. A. Wollack, Z. Wang, M. Pechal, W. Jiang, T. P. McKenna, J. D. Witmer, R. V. Laer, and A. H. Safavi-Naeini, Resolving the energy levels of a nanomechanical oscillator, Nature (London) **571**, 537 (2019).

[49] X. Han, C.-L. Zou, and H. X. Tang, Multimode Strong Coupling in Superconducting Cavity Piezoelectromechanics, Phys. Rev. Lett. **117**, 123603 (2016).

[50] M. Kervinen, J. E. Ramirez-Munoz, A. Valimaa, and M. A. Sillanpaa, Landau-Zener-Stückelberg Interference in a Multimode Electromechanical System in the Quantum Regime, Phys. Rev. Lett. **123**, 240401 (2019).

[51] V. J. Gokhale, B. P. Downey, D. S. Katzer, N. Nepal, A. C. Lang, R. M. Stroud, and D. J. Meyer, Epitaxial bulk acoustic wave resonators as highly coherent multi-phonon sources for quantum acoustodynamics, Nat. Commun. **11**, 2314 (2020).

[52] R. Manenti, A. F. Kockum, A. Patterson, T. Behrle, J. Rahamim, G. Tancredi, F. Nori, and P. J. Leek, Circuit quantum acoustodynamics with surface acoustic waves, Nat. Commun. **8**, 975 (2017).

[53] B. A. Moores, L. R. Sletten, J. J. Viennot, and K. W. Lehnert, Cavity Quantum Acoustic Device in the Multimode Strong Coupling Regime, Phys. Rev. Lett. **120**, 227701 (2018).

[54] K. J. Satzinger, Y. P. Zhong, H.-S. Chang, G. A. Peairs, A. Bienfait, M.-H. Chou, A. Y. Cleland, C. R. Conner, É. Dumur, J. Grebel, I. Gutierrez, B. H. November, R. G. Povey, S. J. Whiteley, D. D. Awschalom, D. I. Schuster, and A. N. Cleland, Quantum control of surface acoustic-wave phonons, Nature (London) **563**, 661 (2018).

[55] L. R. Sletten, B. A. Moores, J. J. Viennot, and K. W. Lehnert, Resolving Phonon Fock States in a Multimode Cavity with a Double-Slit Qubit, Phys. Rev. X **9**, 021056 (2019).

[56] A. Bienfait, K. J. Satzinger, Y. P. Zhong, H.-S. Chang, M.-H. Chou, C. R. Conner, É. Dumur, J. Grebel, G. A. Peairs, R. G. Povey, and A. N. Cleland, Phonon-mediated quantum state transfer and remote qubit entanglement, Science **364**, 368 (2019).

[57] O. Houhou, H. Aissaoui, and A. Ferraro, Generation of cluster states in optomechanical quantum systems, Phys. Rev. A **92**, 063843 (2015).

[58] D. W. Moore, O. Houhou, and A. Ferraro, Arbitrary multimode Gaussian operations on mechanical cluster states, Phys. Rev. A **96**, 022305 (2017).

[59] H. Tan, Y. Wei, and G. Li, Building mechanical Greenberger-Horne-Zeilinger and cluster states by harnessing optomechanical quantum steerable correlations, Phys. Rev. A **96**, 052331 (2017).

[60] O. Houhou, D. W. Moore, S. Bose, and A. Ferraro, Unconditional measurement-based quantum computation with optomechanical continuous variables, arXiv:1809.09733.

[61] C. T. Hann, C.-L. Zou, Y. Zhang, Y. Chu, R. J. Schoelkopf, S. M. Girvin, and L. Jiang, Hardware-Efficient Quantum Random Access Memory with Hybrid Quantum Acoustic Systems, Phys. Rev. Lett. **123**, 250501 (2019).

[62] Y. Chu, P. Kharel, W. H. Renninger, L. D. Burkhart, L. Frunzio, P. T. Rakich, and R. J. Schoelkopf, Quantum acoustics with superconducting qubits, Science **358**, 199 (2017).

[63] G. Andersson, S. W. Jolin, M. Scigliuzzo, R. Borgani, M. O. Tholén, D. B. Haviland, and P. Delsing, Squeezing and correlations of multiple modes in a parametric acoustic cavity, arXiv:2007.05826.

[64] M. Abdi, J.-P. Chou, A. Gali, and M. B. Plenio, Color centers in hexagonal boron nitride monolayers: A group theory and ab initio analysis, ACS Photonics **5**, 1967 (2018).

[65] M. Abdi and M. B. Plenio, Analog quantum simulation of extremely sub-Ohmic spin-boson models, Phys. Rev. A **98**, 040303(R) (2018).

[66] M. Goryachev and M. E. Tobar, Gravitational wave detection with high frequency phonon trapping acoustic cavities, Phys. Rev. D **90**, 102005 (2014).

[67] A. Arvanitaki, S. Dimopoulos, and K. Van Tilburg, Sound of Dark Matter: Searching for Light Scalars with Resonant-Mass Detectors, Phys. Rev. Lett. **116**, 031102 (2016).

[68] M. Abdi, P. Degenfeld-Schonburg, M. Sameti, C. Navarrete-Benlloch, and M. J. Hartmann, Dissipative Optomechanical Preparation of Macroscopic Quantum Superposition States, Phys. Rev. Lett. **116**, 233604 (2016).

[69] W. H. Renninger, P. Kharel, R. O. Behunin, and P. T. Rakich, Bulk crystalline optomechanics, Nat. Phys. **14**, 601 (2018).

[70] S. Kolkowitz, A. C. B. Jayich, Q. P. Unterreithmeier, S. D. Bennett, P. Rabl, J. G. E. Harris, and M. D. Lukin, Coherent sensing of a mechanical resonator with a single-spin qubit, Science **335**, 1603 (2012).

[71] C. A. Muschik, S. Moulieras, A. Bachtold, F. H. L. Koppens, M. Lewenstein, and D. E. Chang, Harnessing Vacuum Forces for Quantum Sensing of Graphene Motion, Phys. Rev. Lett. **112**, 223601 (2014).

[72] P.-B. Li, Z.-L. Xiang, P. Rabl, and F. Nori, Hybrid Quantum Device with Nitrogen-Vacancy Centers in Diamond Cou-

pled to Carbon Nanotubes, Phys. Rev. Lett. **117**, 015502 (2016).

[73] M. Abdi, M.-J. Hwang, M. Aghtar, and M. B. Plenio, Spin-Mechanical Scheme with Color Centers in Hexagonal Boron Nitride Membranes, Phys. Rev. Lett. **119**, 233602 (2017).

[74] M. Abdi and M. B. Plenio, Quantum Effects in a Mechanically Modulated Single-Photon Emitter, Phys. Rev. Lett. **122**, 023602 (2019).

[75] P. Rabl, Cooling of mechanical motion with a two-level system: The high-temperature regime, Phys. Rev. B **82**, 165320 (2010).

[76] F. Galve, L. A. Pachón, and D. Zueco, Bringing Entanglement to the High Temperature Limit, Phys. Rev. Lett. **105**, 180501 (2010).

[77] O. Pfister, S. Feng, G. Jennings, R. Pooser, and D. Xie, Multipartite continuous-variable entanglement from concurrent nonlinearities, Phys. Rev. A **70**, 020302(R) (2004).

[78] A. S. Bradley, M. K. Olsen, O. Pfister, and R. C. Pooser, Bright tripartite entanglement in triply concurrent parametric oscillation, Phys. Rev. A **72**, 053805 (2005).

[79] J. Zhang and S. L. Braunstein, Continuous-variable Gaussian analog of cluster states, Phys. Rev. A **73**, 032318 (2006).

[80] H. J. Briegel, D. E. Browne, W. Dür, R. Raussendorf, and M. Van den Nest, Measurement-based quantum computation, Nat. Phys. **5**, 19 (2009).

[81] M. Kervinen, A. Valimaa, J. E. Ramirez-Munoz, and M. A. Sillanpaa, Sideband Control of a Multimode Quantum Bulk Acoustic System, Phys. Rev. Appl. **14**, 054023 (2020).

[82] G. Adesso and F. Illuminati, Genuine multipartite entanglement of symmetric Gaussian states: Strong monogamy, unitary localization, scaling behavior, and molecular sharing structure, Phys. Rev. A **78**, 042310 (2008).

[83] S. L. Braunstein and C. M. Caves, Statistical Distance and the Geometry of Quantum States, Phys. Rev. Lett. **72**, 3439 (1994).

[84] C. Genes, A. Mari, P. Tombesi, and D. Vitali, Robust entanglement of a micromechanical resonator with output optical fields, Phys. Rev. A **78**, 032316 (2008).

[85] A. Mari and J. Eisert, Gently Modulating Optomechanical Systems, Phys. Rev. Lett. **103**, 213603 (2009).

[86] M. B. Plenio, Logarithmic Negativity: A Full Entanglement Monotone that is Not Convex, Phys. Rev. Lett. **95**, 090503 (2005).

[87] P. Rabl, Photon Blockade Effect in Optomechanical Systems, Phys. Rev. Lett. **107**, 063601 (2011).

[88] H. J. Carmichael, *Statistical Methods in Quantum Optics 1* (Springer-Verlag, Berlin, 1999).

[89] K. Jaehne, K. Hammerer, and M. Wallquist, Ground-state cooling of a nanomechanical resonator via a Cooper-pair box qubit, New J. Phys. **10**, 095019 (2008).

[90] J. R. Johansson, P. D. Nation, and F. Nori, QuTiP: An open-source Python framework for the dynamics of open quantum systems, Comput. Phys. Commun. **183**, 1760 (2012).

[91] G. Adesso, S. Ragy, and A. R. Lee, Continuous variable quantum information: Gaussian states and beyond, Open Syst. Inf. Dyn. **21**, 1440001 (2014).

[92] R. Krischek, C. Schwemmer, W. Wieczorek, H. Weinfurter, P. Hyllus, L. Pezzé, and A. Smerzi, Useful multiparticle entanglement and Sub-Shot-Noise Sensitivity in Experimental Phase Estimation, Phys. Rev. Lett. **107**, 080504 (2011).

[93] P. Hyllus, W. Laskowski, R. Krischek, C. Schwemmer, W. Wieczorek, H. Weinfurter, L. Pezze, and A. Smerzi, Fisher information and multiparticle entanglement, Phys. Rev. A **85**, 022321 (2012).

[94] G. Tóth, Multipartite entanglement and high-precision metrology, Phys. Rev. A **85**, 022322 (2012).

[95] M. G. Genoni and M. G. A. Paris, Quantifying non-Gaussianity for quantum information, Phys. Rev. A **82**, 052341 (2010).